crystals

MDPI

Article

Nanocrystalline Surface Layer of WO_3 for Enhanced Proton Transport during Fuel Cell Operation

Xiang Song [1], Weiqing Guo [2], Yuhong Guo [3], Naveed Mushtaq [4,*], M. A. K. Yousaf Shah [4], Muhammad Sultan Irshad [5,*], Peter D. Lund [6] and Muhammad Imran Asghar [6,7]

1 School of Electronic Engineering, Nanjing Xiaozhuang University, Nanjing 211171, China; songxiang@njxzc.edu.cn
2 Zhijiang College, Zhejiang University of Technology, Shaoxing 312030, China; guowq@zjut.edu.cn
3 Huadong Engineering Corporation Limited, Hangzhou 311122, China; guo_yh@hdec.com
4 Jiangsu Provincial Key Laboratory of Solar Energy Science and Technology, Energy Storage Joint Research Center, School of Energy and Environment, Southeast University, Nanjing 210096, China; alikamranshah91@gmail.com
5 School of Materials Science and Engineering, Hubei University, Wuhan 430062, China
6 New Energy Technologies Group, Department of Applied Physics, Aalto University School of Science, Aalto, FI-00076 Espoo, Finland; peter.lund@aalto.fi (P.D.L.); imran.asghar@aalto.fi (M.I.A.)
7 Hubei Collaborative Innovation Center for Advanced Organic Chemical Materials, Faculty of Physics and Electronic Science, Hubei University, Wuhan 430062, China
* Correspondence: mahrnaveedm65@gmail.com (N.M.); sultan.danish93@gmail.com (M.S.I.); Tel.: +86-159-2761-7592 (N.M.); +86-156-2313-8982 (M.S.I.)

check for updates

Citation: Song, X.; Guo, W.; Guo, Y.; Mushtaq, N.; Shah, M.A.K.Y.; Irshad, M.S.; Lund, P.D.; Asghar, M.I. Nanocrystalline Surface Layer of WO_3 for Enhanced Proton Transport during Fuel Cell Operation. *Crystals* **2021**, *11*, 1595. https://doi.org/10.3390/cryst11121595

Academic Editors: Avishek Karmakar, Samrat Ghosh and Vladislav V. Kharton

Received: 27 November 2021
Accepted: 18 December 2021
Published: 20 December 2021

Publisher's Note: MDPI stays neutral with regard to jurisdictional claims in published maps and institutional affiliations.

Copyright: © 2021 by the authors. Licensee MDPI, Basel, Switzerland. This article is an open access article distributed under the terms and conditions of the Creative Commons Attribution (CC BY) license (https://creativecommons.org/licenses/by/4.0/).

Abstract: High ionic conductivity in low-cost semiconductor oxides is essential to develop electrochemical energy devices for practical applications. These materials exhibit fast protonic or oxygen-ion transport in oxide materials by structural doping, but their application to solid oxide fuel cells (SOFCs) has remained a significant challenge. In this work, we have successfully synthesized nanostructured monoclinic WO_3 through three steps: co-precipitation, hydrothermal, and dry freezing methods. The resulting WO_3 exhibited good ionic conductivity of 6.12×10^{-2} S cm^{-1} and reached an excellent power density of 418 mW cm^{-2} at 550 °C using as an electrolyte in SOFC. To achieve such a high ionic conductivity and fuel cell performance without any doping contents was surprising, as there should not be any possibility of oxygen vacancies through the bulk structure for the ionic transport. Therefore, laterally we found that the surface layer of WO_3 is reduced to oxygen-deficient when exposed to a reducing atmosphere and form $WO_{3-\delta}/WO_3$ heterostructure, which reveals a unique ionic transport mechanism. Different microscopic and spectroscopic methods such as HR-TEM, SEM, EIS, Raman, UV-visible, XPS, and ESR spectroscopy were applied to investigate the structural, morphological, and electrochemical properties of WO_3 electrolyte. The structural stability of the WO_3 is explained by less dispersion between the valence and conduction bands of $WO_{3-\delta}/WO_3$, which in turn could prevent current leakage in the fuel cell that is essential to reach high performance. This work provides some new insights for designing high-ion conducting electrolyte materials for energy storage and conversion devices.

Keywords: fuel cell; solid oxide fuel cell; monoclinic WO_3 electrolyte; dry freezing method; proton conduction; spectroscopic analysis

1. Introduction

Fuel cells (FCs) provide a clean and efficient way to generate electricity from H_2 and hydrocarbon fuels. Due to high operating temperatures, solid oxide fuel cells (SOFCs) can also be used in combined heat and power applications. One of the main challenges for SOFCs is developing high oxygen ion (O^{2-}) conductivity of electrolyte materials. Structural doping has been remained a general methodology for developing high ionic conductivities [1,2]. In this methodology, the host cations could often be replaced by a

lower valence state, which produces an oxygen-deficient structure to conduct O^{2-} (For example, Zr^{4+} or Ce^{4+} are replaced with Y^{3+} and Sm^{3+}) [3,4]. However, this approach does not significantly enhance fuel cell performance at low operating temperatures due to limited ionic conductivity [4].

Protonic conducting fuel cells (PCFCs), a sub-class of SOFCs, have emerged with great potential for lowering the operating temperature to the range of 400–700 °C. PCFCs can achieve higher fuel utilization by producing the water on the cathode side and avoiding fuel dilution effectively [5]. Another advantage of PCFCs is that many proton-conducting electrolytes such as $BaZr_{0.8}Y_{0.2}O_{3-\delta}$, $BaZr_{0.1}Ce_{0.7}Y_{0.2}O_{3-\delta,}$ and Yb-doped $BaZr_{0.1}Ce_{0.7}Y_{0.2}O_{3-\delta}$ offer high protonic conductivity at an intermediate operating temperature of 600–800 °C [6–8]. Further reduction of the operating temperature, (e.g., 400–600 °C) reduces the power output sharply. If PCFCs could operate in the range of 400–600 °C, it would help prolong the lifetime. The main critical obstacle to achieving high-performance low-temperature PCFCs is the limited proton conductivity of the electrolyte and cathode materials for oxygen reduction reaction (ORR), both of them perform poorly at low temperatures [9–14].

However, obtaining the benchmark in proton conductivity (H^+) for electrolytes and their chemical stability is a big challenge. The best proton-conducting electrolytes, such as doped barium cerates ($BaCeO_{3-\delta}$), lead to poor CO_2 tolerance and rapid decomposing due to forming carbonates at a temperature higher than 600 °C, which is a significant limitation for their use in the device [15]. Recently, next-generation proton-conducting electrolytes such as MTO_4, where M = lanthanide/alkali metals and T = Nb, W, Mo, Mn, shows high CO_2 tolerance [16,17]. Moreover, the semiconductor-based electrolyte has been reported to deliver the best performance at a low operating temperature [10–14]. The doped $BaCeO_{3-\delta}$ only exhibits dominant H^+ conductivity under wet conditions or reduced atmosphere and shows significant p-type conductors under oxidizing conditions [15]. WO_4/WO_3 based materials almost remain pure H^+ conductors in both wet and oxidizing conditions, although they exhibit moderate H^+ conductivity. However, WO_3 to be a direct bandgap semiconductor with less disseminative valence and conduction bands has shown considerable interest for multiple applications in energy devices. WO_4/WO^{3-} type oxides exhibit a high oxide ion conduction, e.g., $Pb_{0.9}Sm_{0.1}WO_{4+\delta}$ shows a conductivity of $\sim 2 \times 10^{-2}$ S cm^{-1} at 800 °C, which is comparable to that of YSZ (3.6×10^{-2} S cm^{-1} at 800 °C) [18].

Controlling grain boundary conduction (GBs) into nanocrystalline material is an emerging field. Therefore, we have synthesized nanocrystalline WO_3 in three steps to obtain the fine morphology to effectively modulate its electrical properties. We have synthesized nano-structure WO_3 by combining three steps following one by one, such as (i) co-precipitation, (ii) hydrothermal, and (iii) dry freezing method. The structural, chemical and morphological analysis of prepared WO_3 powders is analyzed. However, in situ formations of $WO_{3-\delta}/WO_3$ heterostructure when exposed to H_2- side in the fuel cell that could help migrate ions accompanied with the creation of the internal cavity (charge accumulation and depletion region) could be explained by the "surface locking" effect. The prepared WO_3 spontaneously facilitated ionic transport exhibiting high ionic conductivity of 6.12×10^{-2} S cm^{-1} and excellent power density of 478 mW cm^{-2} at 550 °C. The results demonstrate that the approach proposed is helpful for developing new materials with unique functionalities for advanced PCFCs/SOFCs.

2. Materials and Methods

2.1. Material Preparation Methods

The powders of WO_3 were prepared in three steps. Initially, an appropriate amount of ammonium tungstate with a chemical formula of $(NH_4)10H_2(W_2O_7)_6$ was bought from Shanghai Macklin Biochemical Co., Ltd., Shanghai, China (purity 98.5%) was dissolved into deionized water to prepare the 0.5 mol/L solutions. In parallel, the 1 mol/L of Na_2CO_3 was prepared into 100 mL water; afterward, the Na_2CO_3 solution was added dropwise

to the above solution under continuous stirring resulted in white milky precipitates. The obtained precipitates were moved to a Teflon autoclave bottle for hydrothermal treatment at 180°C for 6 h at 180 in a vacuum oven. Afterward, the precipitates were collected to wash and filter numerous times with distilled water and absolute ethanol to eliminate surface-adsorbed water. The resultant precursors were dry freezes at −40 °C for 4 h. Furthermore, it was followed by a vacuum at 1.0 P to cool down to room temperature to remove the absorbed water. Moreover, obtained powders were calcined at 750 °C for 6 h to obtain WO_3 nanoparticles. Furthermore, tungsten trioxide (WO_3) purchased from Shanghai Macklin Biochemical Co., Ltd., Shanghai, China (99.8%) was used for comparative study to synthesize WO_3.

2.2. Material Characterizations and Electrochemical Measurements

The Bruker D8 advanced X-ray diffractometer (Bruker, Hanau, Germany, with Cu Kα radiation, λ = 1.5418 Å) was employed to study the crystalline structure of the synthesized WO_3 powders in 2θ ranges from 10–70°. Furthermore, crystal structure, microstructure, and chemical composition of prepared WO_3 were studied via FEI Tecnai GI F30 and JEOL JSM7100F (resolution transmission electron microscopy; HR-TEM and field emission scanning electron microscope). X-ray photoelectron spectroscopy (XPS, Physical Electronics Quantum 2000, Al Kα X-ray source) was engaged for chemical oxidation states where the raw data was analyzed through CASA XPS software. Raman spectra were carried out on NT-MDT (Russia) Raman spectrometer at room temperature, with 532 nm solid-state laser as the excitation source and laser power of 20 mW. The UV-Vis 3600 spectrophotometer was used to measure the absorbance spectrum. The electron spin resonance (ESR) measurements were performed using JES X320 (JEOL). Keithley 2400 source meter was used to measure dc-four probed method conductivity.

2.3. Fuel Cells Fabrication and Electrochemical Measurements

We utilized the dry-pressing method to fabricate the SOFC cell with dense electrolyte and porous electrodes. The WO_3 powder was pressed between the symmetrical electrodes of $Ni_{0.8}Co_{0.15}Al_{0.05}LiO_{2-\delta}$ (NCAL) to form the electrolyte membranes as thin as 285 μm using low filling density powders. In detail used as an electrode was purchased from Bamo Sci. & Tech. Joint Stock Company Ltd., Tianjin, China. In detail, a slurry of NCAL was prepared and painted on porous Ni-foam followed by drying at 120 °C for 2 h. The synthesized and commercially purchased WO_3 powders were pressed between the prepared NCAL electrodes under 240 MPa to produce the solid cells. The designed fuel cell pellet's diameter, thickness, and active area were about 13 mm, 1.5 mm, and 0.64 cm^2, respectively. DC electronic load instrument (ITECH8511, ITECH Electrical Co., Ltd., New Taipei, Taiwan) was employed to determine the fuel cell performance of fabricated cells under the H_2 as fuel and air as an oxidant with a flow rate of 100–110 mL/min and 100 mL/min, respectively. The I-V (current density-voltage) and I-P (current density–power density) were recorded to present the electrochemical characteristics of the prepared FC devices. Electrochemical impedance spectroscopy (EIS) was measured by Gamry Reference 3000, USA workstation under the fuel cell open-circuit voltage (OCV) conditions in the frequency range of 0.1 to 106 Hz with 10 mV of dc signal. ZSIMPWIN software was used to fit the model circuit with obtained EIS data.

3. Results & Discussion

3.1. Structural and Compositional Study

Figure 1a shows the XRD pattern of WO_3, whose main diffraction peaks are located at 2θ° of the 22.8, 23, 24, 26, 28, 33, 33.5, 34.5, 41, 50.5, 56, which are corresponding to (002), (020), (200), (120), (112), (202), (022), (220), (222), (232) and (114) planes of monoclinic crystal structure of WO_3 (JCPDS no 43–1035), with space group Pi (C~), and lattice of a = 7.309, b = 7.522, c = 7.678, α = 88.81, β = 90.92, γ = 90.93. There are no extra peaks observed in the patterns, eliminating the possibility of additional phase formation except the monoclinic

WO_3 phase. To verify crystallography of synthesized WO_3, Nano-STAR (Bruker-AXS was used to measure the wide-angle scattering. Figure 1b,c shows a wide-angle plot in the 2θ range from 2°–45° and its corresponding 3-D mapping image, respectively. The wide-angle confirms the high purity monoclinic crystal structure of WO_3 measured by XRD. Moreover, the crystallographic structure of WO_3 is confirmed by HR-TEM, as shown in Figure 1d,e. The d-spacing values calculated using a digital micrograph are 0.236 and 0.213 nm, which can be nominated to (200) and plane (020) planes, respectively. These planes could also be confirmed by a selected area electron diffraction (SAED) pattern, as shown in Figure 1f [19,20].

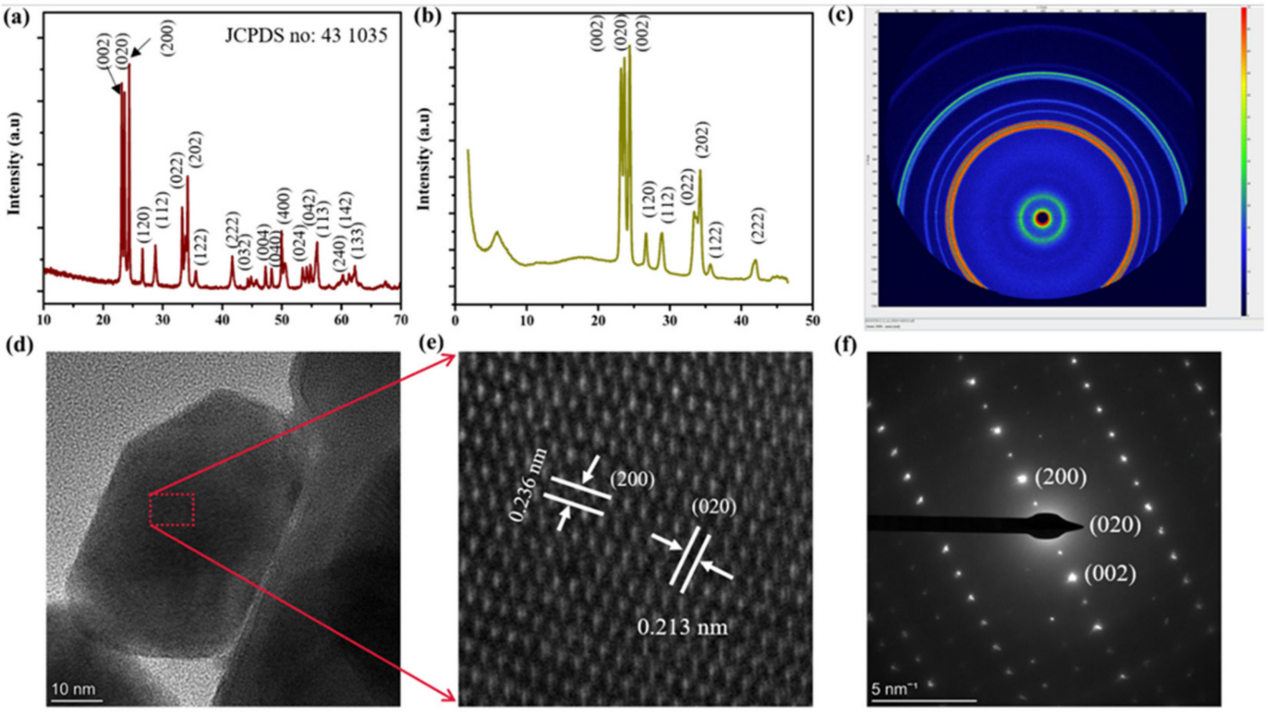


Figure 1. Structure characterization (**a**) X-ray diffraction pattern of synthesized WO_3; (**b**,**c**) wide-angle X-ray diffraction pattern and its corresponding mapping for the lattice fringes image of WO_3; (**d**,**e**) crystal structure and d-spacing of WO_3 measured by HR-TEM and (**f**) selected area electron diffraction (SAED) pattern of the synthesized WO_3.

Figure 2 shows nano-scaled HR-TEM and s STEM images for synthesized WO_3, where sophisticated and fine nano-particles with a particle size of <50 nm can be seen clearly. The restrain of agglomerates and the growth of particles in WO_3 can be attributed to the purification of the synthesis method we have used. Moreover, a line scan using high-angle annular dark-field scanning transmission electron microscopy (HAADF-STEM) was used to confirm the elemental distribution at the particle level. Figure 2c shows a HAADF-STEM image with elements mapping of W and O, where a homogenous chemical distribution can be observed. Figure 2d shows the chemical distribution along with the line scan compared to the HAADF image in the 0–100 nm range. Figure 3f shows the energy dispersive spectroscopy (EDS) image measured using the HAADF-STEM image. The results mentioned above manifest that the particles are at nano-level and are well connected, which leads to enhancement of the surface area with more active sties to enhance the overall performance of fuel cell devices [21,22].

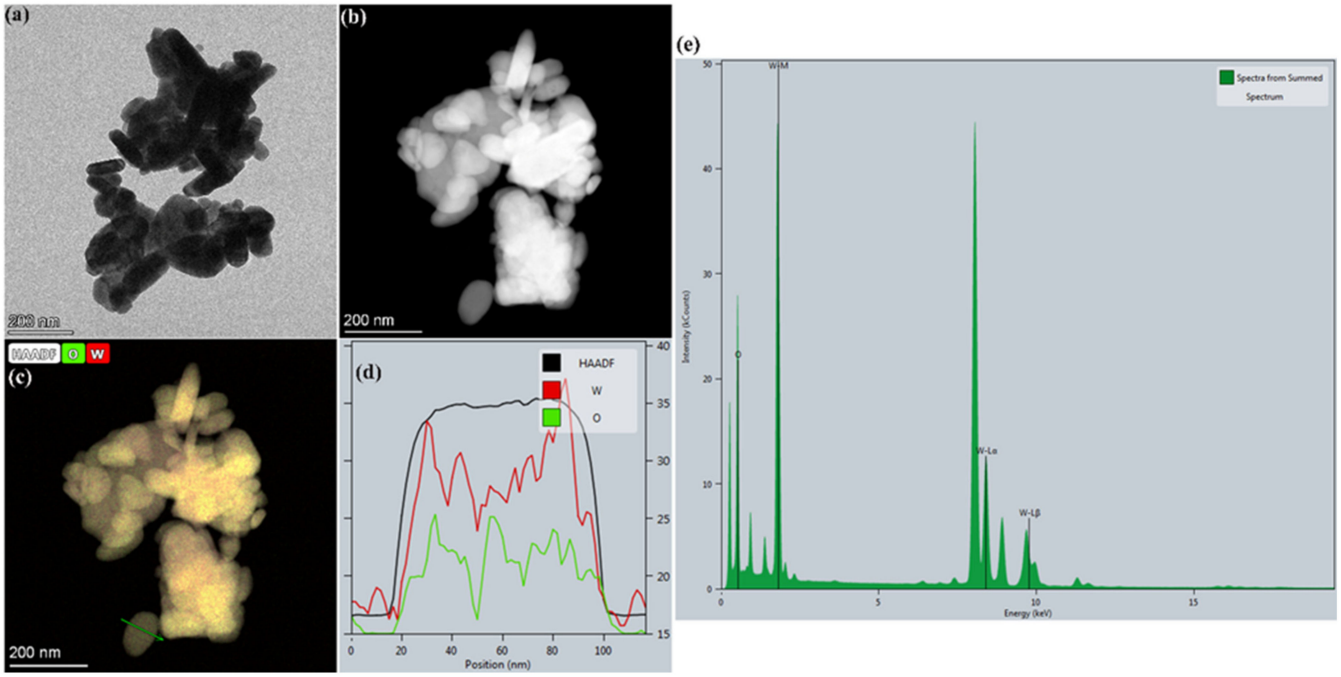


Figure 2. Morphology and compositional characterization (**a**) HR-TEM image of WO_3; (**b**) STEM image of synthesized WO_3; (**c**) STEM-HAADF elements mapping for W and O; (**d**) line scan distribution of WO_3 corresponding to HAADF; (**e**) EDS image of WO_3 for actual chemical composition study.

3.2. Electrochemical Performance Measurements

The electrochemical performance of the prepared WO_3 in comparison to commercially purchased WO_3 in a fuel cell as an ion-conducting electrolyte was evaluated. Figure 3a displays typical current-voltage (I–V) and corresponding power density (I-P) characteristics of fuel cells using commercial WO_3 and our synthesized WO_3 material as an electrolyte at 450–550 °C. The OCV of 1.03 V and the maximum power density (Pmax) of 418 ± 2% mW cm^{-2} were achieved for our prepared WO_3 electrolyte, while commercially purchased WO_3 exhibited (Pmax) of only 260 mW cm^{-2}. The OCV (e.g., 1.03 V at 550 °C) agrees with the Nernst theoretical potential at this temperature, showing that the ionic transfer number is near unity and WO_3 acts electronically insulating [23–25]. Moreover, our synthesized WO_3 electrolyte fuel cell displayed good electrochemical performance even at low temperatures, as shown in Figure 3b. It exhibited peak power densities of 360 and 310 mW cm^{-2} at 500 °C and 450 °C, respectively. The enhanced electrochemical performance of synthesized WO_3 over commercially purchased WO_3 suggests the vital role of synthesis method and nanostructured morphology, where the surface layer of WO_3 can easily be reduced and produce the strong $WO_{3-\delta}/WO_3$ heterostructure for creating the surface path for easy transport of H^+ when it's exposed to H_2 in fuel cell conditions [20]. During the online electrochemical process, the prepared WO_3 material could facilitate the better intercalation of protons because of the high surface-active area and easy reduction of the surface layer. Therefore, obtained results suggested that the nanostructured stoichiometry synthesized by three steps synthesis could be helpful to control the surface structural properties. In this way, the WO_3 surface kinetically favors the heterolytic dissociation of H_2 to form W–H and O–H species. The resulting W–H further evolves to the thermodynamically more stable O–H species, accompanied by the reduction of W^{6+} to W^{5+} into the surface layer.

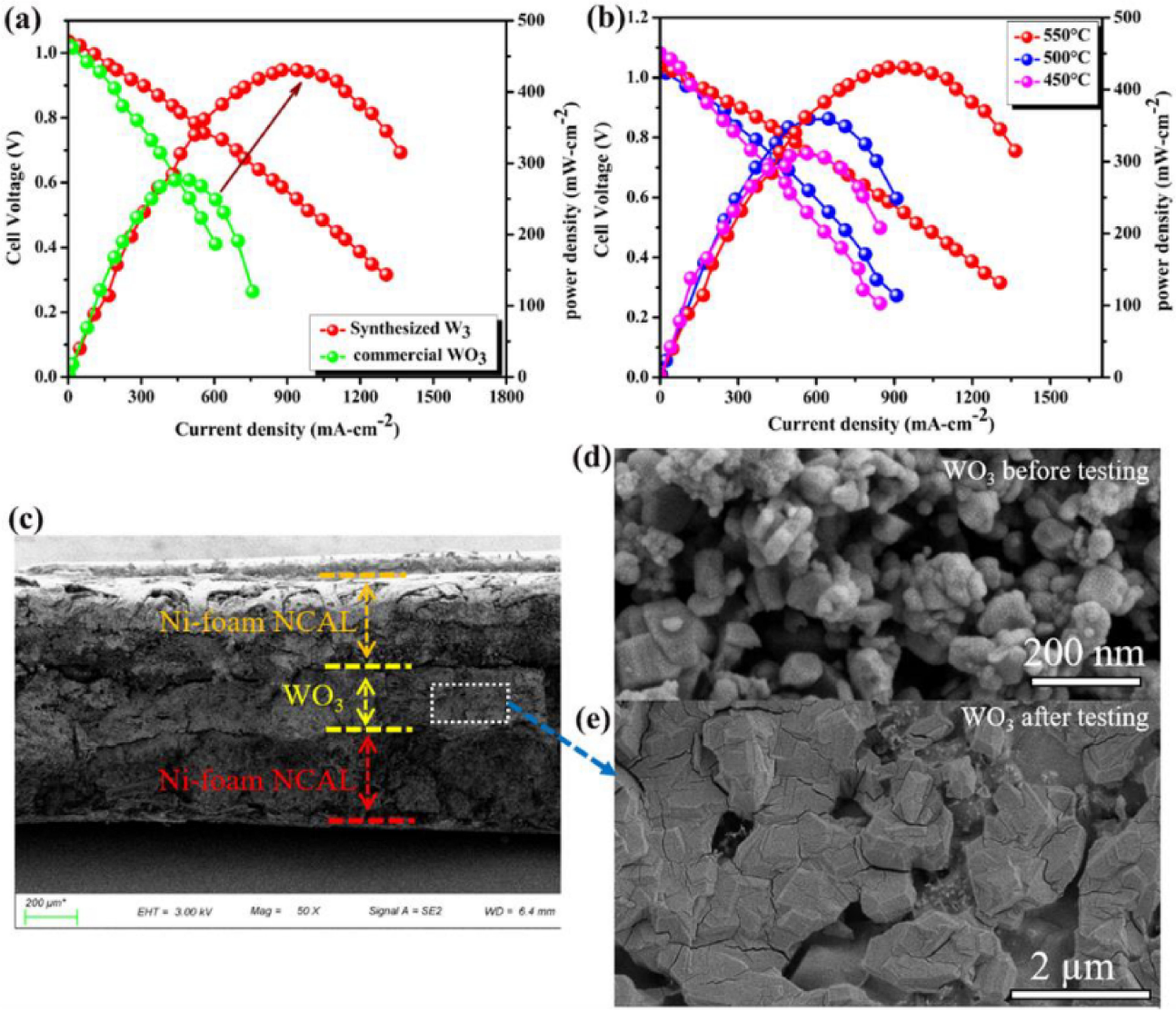


Figure 3. Electrochemical performance characterizations: (**a**) typical current (I)–voltage (V) characteristics curves of using our synthesized material (WO_3) and commercially purchased WO_3 as an electrolyte in fuel cell operating at 550 °C; (**b**) fuel cell using our synthesized WO_3 as an electrolyte at different operating temperatures of 450–550 °C; (**c**) tri-layer cross-sectional SEM images of anode supported symmetrical fuel cell with our synthesized WO_3 electrolyte after performing the electrochemical test; (**d**,**e**) enlarged SEM image of WO_3 electrolyte layer, before and after fuel cell testing, respectively.

Additionally, Figure 3c shows a typical cross-sectional scanning electron microscopy (SEM) image of the fuel cell with WO_3 acquired after online sintering and test. The SEM image indicates that the WO_3 electrolyte layer appears fully dense, without noticeable connected pores, and appears well-adhered to the anode substrate, without any cracking or delamination after fuel cell testing as compared with before testing (Figure 3d,f). Such adhesive and dense structure of WO_3 electrolyte guarantee better fuel cell performance [23,26].

3.3. Electrochemical Impedance and Electrical Conductivity

Further, EIS characterizations were performed for the cell with synthesized WO_3 electrolyte in both air and H_2/air atmosphere at 450–550 °C under OCV conditions. Figure 3a,b shows Nyquist curve of the measured EIS spectra and Fitted data using ZSIMPWIN software with equivalent circuit modeling of R_o-(R_1-CPE_1) − (R_2-CPE_2), where R_o, is the ohmic resistance from the electrolyte, R_1 and R_2 belong to charge transfer and mass transfer losses of the fuel cell with WO_3 electrolyte, respectively. It can be seen from the EIS spectra of

Figure 4a,b that R_o of the fuel cell with WO_3 dramatically reduced in H_2/air (fuel cell operating conditions) as compared to in the air. For example, fuel cell with WO_3 electrolyte exhibited R_o of only 1.09 Ω cm^2 in H_2/air at 550 °C, while in the air it shows 12.85 Ω cm^2 Similarly, a clear difference in R_o values at a low operating temperature of 500 and 450 °C also can be visualized. These results describe that when WO_3 is exposed to the H_2 atmosphere, its surface could be reduced to W^{5+} to form $WO_{3-\delta}/WO_3$, and protons can easily be transported through this layer as reported for CeO_2. Afterward, it breaks the accumulation layer at the interface of electrode/electrolyte and hence reduces the charge transfer resistance (R_1), mass transport resistance (R_2) of fuel cells, as shown in Figure 4a,b. The decrease in charge transfer resistance at the interface of electrolyte/electrode for each cell may be followed by value capacitance for that cell (i.e., $R_1 \sim C_1$, $R_2 \sim C_2$), where capacitance can be determined by $C_i = \left(\frac{R_i Q_i^{\frac{1}{n}}}{R_i}\right)$, where R is corresponding resistance and n to Frequency power [$0 \geq n \leq 1$] of the Q's values [11]. The cell's charge transfer resistance in H_2/air compared to EIS spectra in air decreases from 10.5 to 0.17 Ω cm^2, followed by a decline in space charge capacitance from 1.231 × 10^{-3} F to 1.713 × 10^{-5} F at 550 °C [24,25,27].

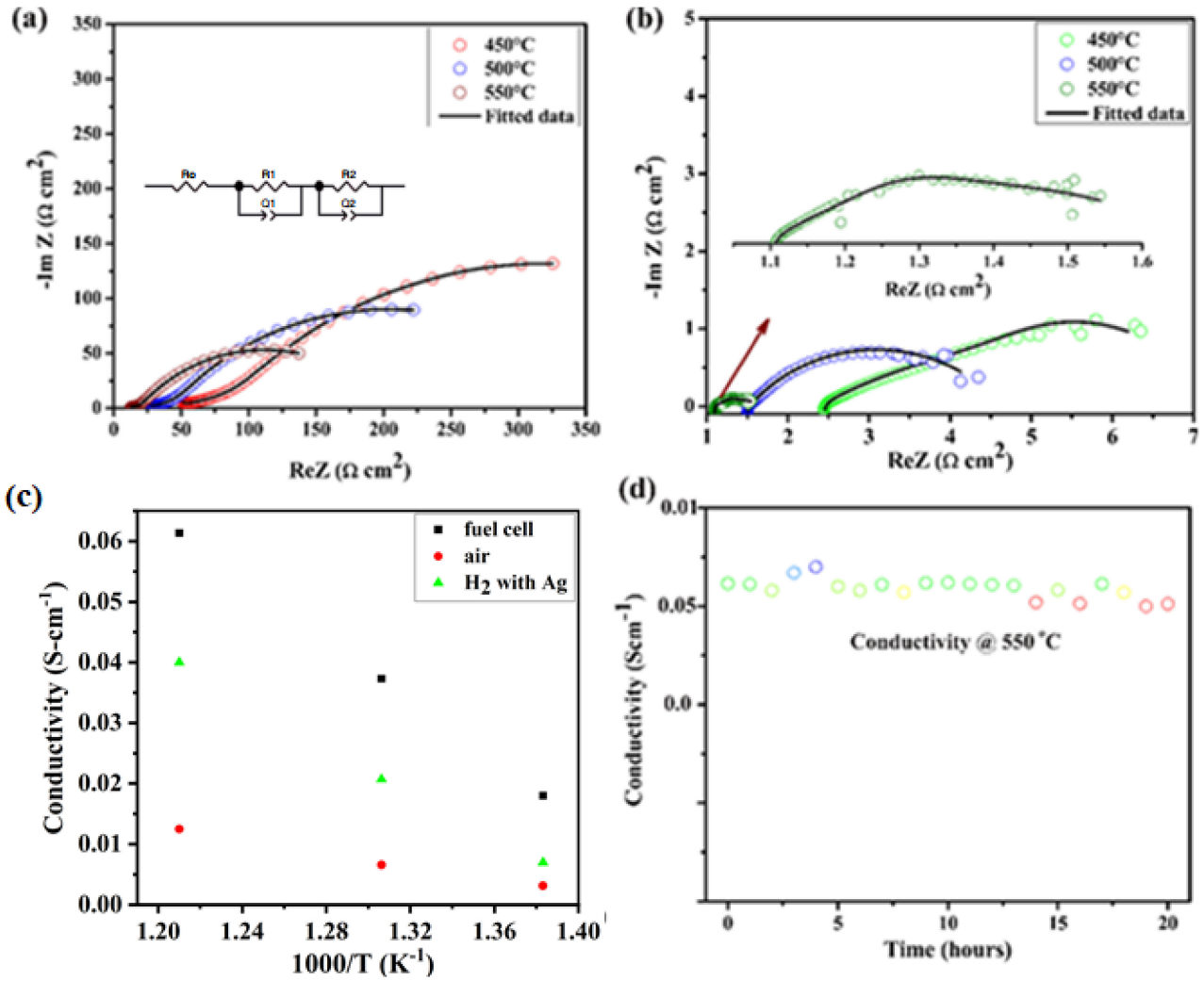


Figure 4. (**a**) Impedance spectra for the fuel cell with synthesized WO_3 electrolyte layer measured in air at 450–550 °C and the corresponding fitting data; (**b**) impedance spectra for the fuel cell with synthesized WO_3 electrolyte layer measured in H_2/air at 450–550 °C; (**c**) comparison of the ionic conductivity of WO_3 measured in air and H_2 atmosphere with NCAL and electrodes and (**d**) stability of ionic conductivity measured over 24 h.

The ionic conductivity of synthesized WO_3 in both air and H_2/air was calculated using R_o values of the fitted data. As shown in Figure 4c, the ionic conductivity of synthesized WO_3 in H_2/air is much higher than only in air atmospheres. The synthesized WO_3 exhibits the ionic conductivity of 6.12×10^{-2} S cm^{-1} in H_2, while in the air, only 1.21×10^{-3} S cm^{-1}. The conductivity results support our findings that the WO_3 surface could be reduced to deficient $WO_{3-\delta}$ and support fast protonic transport. Moreover, cell ionic conductivity was measured over 24 h to check its behavior, and it shows the stable ionic conductivity as can be seen in Figure 4d. Furthermore, the proton conductivity of WO_3 was measured using Ag current collectors in H_2 without using the NCAL electrode. In these conditions, WO_3 shows a little lower proton conductivity as compared to fuel cell conditions (Figure 4c). However, these results indicate that WO_3 synthesized by three-step methods could be a good candidate for electrolyte application in advanced SOFCs [20].

3.4. Spectroscopic Analysis

Moreover, different spectroscopic techniques, such as Raman, UV-visible, and X-ray photoelectron spectroscopies, were employed to study further structural properties of WO_3 powders before and after fuel cell measurements. Figure 5a displays specific Raman shifts bands for synthesized WO_3 centered at 266, 322, 709, and 803 cm^{-1} links to the stretching vibrations of (O-W-O), (O-W-O), (W_2O_6 & W_3O_8), and (W-O-W) from 200–2400 Raman shifts/cm^{-1}. After performing fuel cell measurements, a small redshift of 0.5 cm^{-1} in the Raman shift band of WO_3 was observed. However, overall, WO_3 shows good structure stability after fuel cell measurements. Moreover, UV-Visible absorbance spectra of WO_3 for before and after fuel cell performance measurements are presented in Figure 5b. There is just a little bit of difference in absorbance spectra that can be observed. The difference in absorbance spectra is an obvious indicator for lower down in the energy band gap of WO_3, which only could be due to the reducing the surface and producing oxygen vacancies. The low energy gap will help to improve the ionic conductivity and, hence, better fuel cell performance [21,24,25,28].

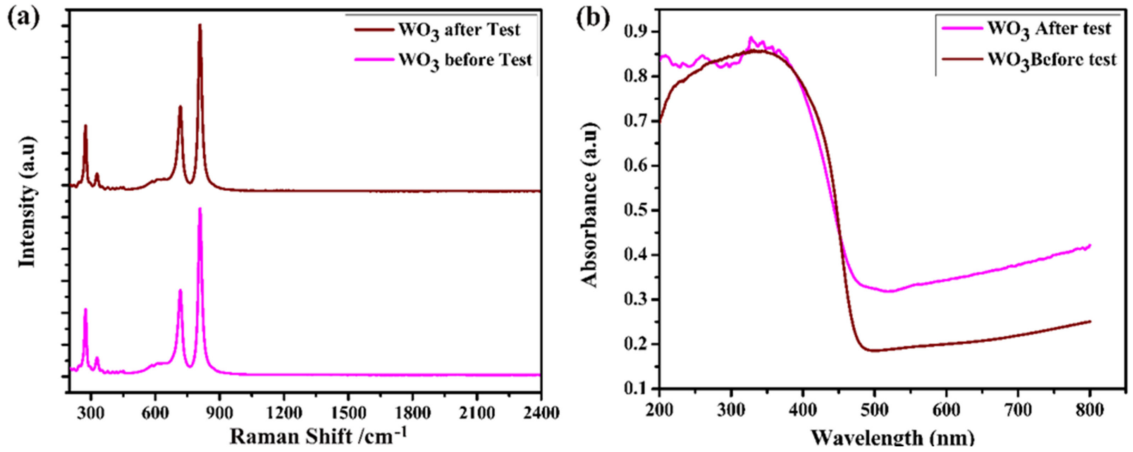


Figure 5. (**a**,**b**) Raman and UV-visible spectra of as-synthesized WO_3 powders and for WO_3 after fuel cell performance measurements.

High-resolution XPS spectra of as-synthesized WO_3 powders are shown in Figure 6a,b. After subtracting Shirley's background, high-resolution XPS spectra were fitted by the mixture function of Lorentzian and Gaussian. Our focus was to observe the chemical and electronic state configuration changes of W-4f and O1s spectra before and after electrochemical performance measurements. Figure 6a shows the XPS spectra of 4f-W^{6+} (5/2, 7/2) and 4-f W^{5+} (5/2, 7/2) that appear at 35.32/37.52 and 35.7/38.05 eV, whereas in after fuel cell performance measurements at 35.12/37.22 and 35.9/37.85 eV. These downshifts in B.E of W^{6+} 4f (5/2, 7/2) and W5 + 4f (5/2, 7/2) manifest a reduction in WO_3 after fuel cell measurements. Moreover, O1s spectra of the material also influence the ionic conductivity

of a material [29,30]. The O1s spectra after fuel cell measurements contain lattice oxygen (lattice O^{2-}) and oxygen vacancy peaks, as shown in Figure 6b. The O1s spectra of WO_3 after fuel cell measurements display two partially superimposed peaks (Figure 6b). There are two significant excitations: the first includes O1s of lattice oxygen bands and the second, $WO_{3-\delta}$ band with binding energy (BE) ranging from 528 to 533.5 eV [28,29]. The low BE peak at 529.2 can be ascribed to the lattice oxygen (O Lattice), higher at 531.4- to extra oxygen vacancies. The increased area percentage ratio of O_{lat}/O_{vac} of WO_3 after fuel cell measurements indicates high oxygen vacancies concentration, which plays an essential role in high fuel cell performance [21,28]. However, these results provide clear evidence that an in situ surface reduction produces oxygen vacancies for the fast protons transports, as shown in Figure 6c. Therefore, our developed strategy could help create high-performance LT-SOFCs electrolyte materials in a new way [31]. The XPS data shows that W4f and O1s percentage is different (W4f−18.37; O1s 56.65%) as compared to as synthesized sample (W4f−20.5; O1s 54.26). It means the after the fuel cell performance measurements the WO_3 has more oxygen vacancies than as pristine WO_3. Furthermore, electron spin resistance (ESR) configures the change in structural properties after fuel cell measurements. Figure 6c shows the full spectrum of proton unirradiated WO_3 and proton irradiated WO3 phases. Where proton irradiation-induced defect phase lines and the well-resolved group of the ESR spectrum can be seen after fuel cell measurements. However, ESR results confirm our proposed mechanism that the surface layer of WO_3 is reduced during the in-situ operation of the fuel cell, and it facilitates proton transport.

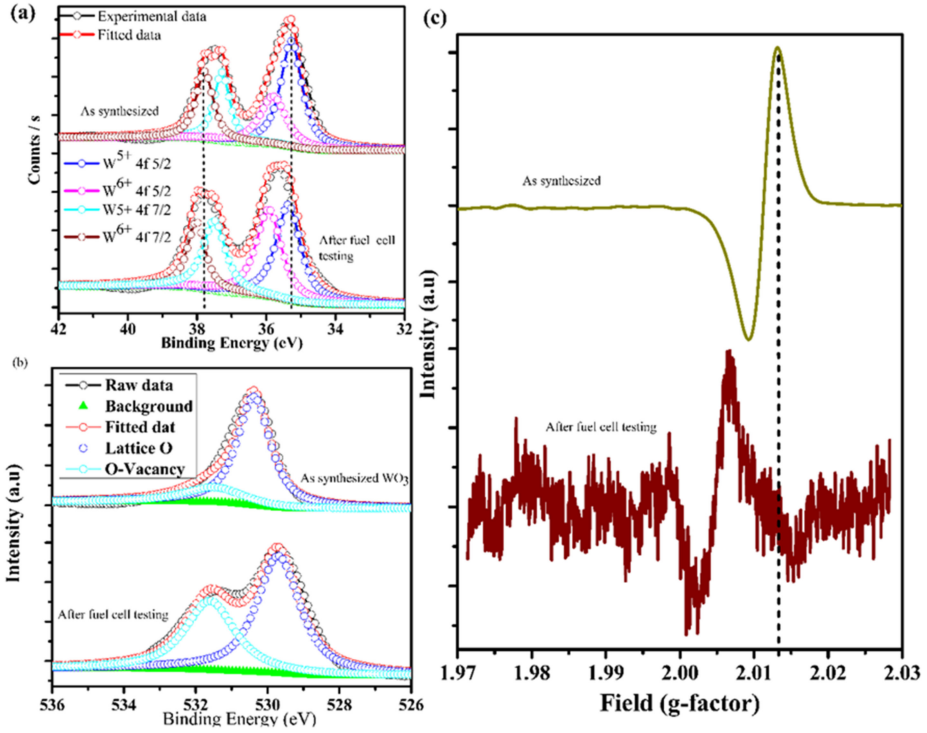


Figure 6. (**a**) X-ray photoelectron spectra of (**a**,**b**) W-4f and O1s spectra of WO_3 for as-synthesized WO_3 powders and after fuel cell performance measurements; (**c**) electron spinning resonance (ESR) study of as-synthesized WO_3 and after fuel cell measurements.

The schematic diagram of the process involved for pristine WO_3 to deficient $WO_{3-\delta}$ layer formation for migration of oxygen and proton ions is shown in Figure 7. The proton transport is accompanied by a surface layer of $WO_3/WO_{3-\delta}$ as shown in the last step of Figure 7.

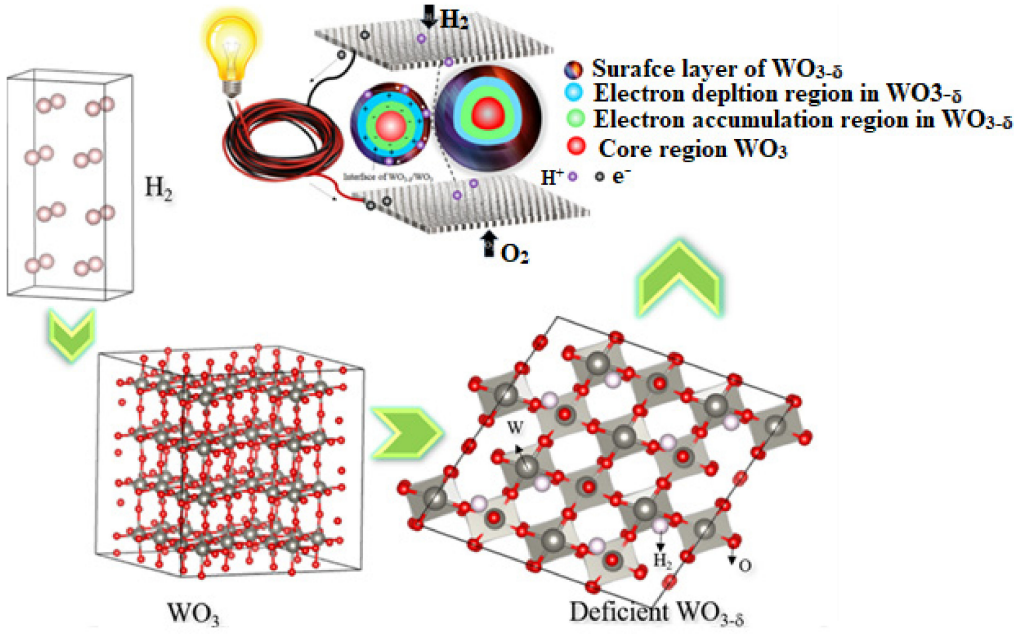


Figure 7. The different processes involved in the phase transition of WO_3 to $WO_{3-\delta}$ and schematic of our proposed proton transport mechanism in WO_3 during fuel cell operation.

4. Conclusions

In summary, we have successfully synthesized and characterized WO_3 nanostructured material by combining three synthesis methods. Furthermore, the synthesized nanostructured WO_3 with a monoclinic structure demonstrated excellent proton conductivity during fuel cell operation. The ionic conductivity reached 6.12×10^{-2} S cm^{-1} in an H_2 atmosphere as compared to 1.21×10^{-3} S cm^{-1} in the air. The fabricated fuel cell using prepared WO_3 as elect4rolyte exhibited a high-power density of 418 mW cm^{-2} at 550 °C. Furthermore, we used different microscopic and spectroscopic analyses to study the mechanism behind the drastic increase in ionic conductivity of WO_3 during fuel cell operation. We found that synthesized nanostructured WO_3 surfaces can easily be reduced to form an oxygen-deficient layer and facilitate protons transport effectively when exposed to a reduction in the atmosphere. The ex-situ spectroscopies that included Raman, UV-visible, XPS, and ESR clearly described our findings and the structural change properties of WO_3 during the fuel cell operation. In conclusion, this method could form the basis of interest to develop new WO_3 based proton-conducting electrolytes, which could be useful for all energy devices and material systems.

Author Contributions: N.M. provided the concept of this study; X.S. performed the experiments and wrote the first draft; W.G. and Y.G. contributed to the data curation; M.A.K.Y.S. and M.S.I. conducted the formal analysis of the results and the manuscript; P.D.L. and M.I.A. helped to revise the manuscript. All authors have read and agreed to the published version of the manuscript.

Funding: School of Electronic Engineering, Nanjing Xiaozhuang University, 211171 Nanjing, China for providing experimental facilities. Further, this work was supported by National Natural Science Foundation of China (NSFC) under the grant #51772080 and 11604088 and Southeast University (SEU PROJET # 3203002003A1). Dr. Asghar thanks the Hubei Talent 100 program and Academy of Finland (grant no. 13329016 and 13322738) for their support.

Acknowledgments: Authors Acknowledged School of Electronic Engineering, Nanjing Xiaozhuang University, 211171 Nanjing, China for providing experimental facilities and publication charges.

Conflicts of Interest: The authors declare that they have no known competing financial interests or personal relationships that could have appeared to influence the work reported in this paper.

References

1. Duan, C.; Kee, R.J.; Zhu, H.; Karakaya, C.; Chen, Y.; Ricote, S.; Jarry, A.; Crumlin, E.J.; Hook, D.; Braun, R.; et al. Highly durable, coking and sulfur tolerant, fuel-flexible protonic ceramic fuel cells. *Nature* **2018**, *557*, 217–222. [CrossRef] [PubMed]
2. Choi, S.; Kucharczyk, C.J.; Liang, Y.; Zhang, X.; Takeuchi, I.; Ji, H.-I.; Haile, S.M. Exceptional power density and stability at intermediate temperatures in protonic ceramic fuel cells. *Nat. Energy* **2018**, *3*, 202–210. [CrossRef]
3. Malavasi, L.; Fisher, C.A.J.; Islam, M.S. Oxide-ion and proton conducting electrolyte materials for clean energy applications: Structural and mechanistic features. *Chem. Soc. Rev.* **2010**, *39*, 4370–4387. [CrossRef]
4. Goodenough, J.B. Oxide-Ion Conductors by Design. *Nature* **1999**, *404*, 821–823. [CrossRef]
5. Zhang, L.; Chae, S.-R.; Hendren, Z.; Park, J.-S.; Wiesner, M.R. Recent advances in proton exchange membranes for fuel cell applications. *Chem. Eng. J.* **2012**, *204–206*, 87–97. [CrossRef]
6. Bi, L.; Da'As, E.H.; Shafi, S.P. Proton-conducting solid oxide fuel cell (SOFC) with Y-doped $BaZrO_3$ electrolyte. *Electrochem. Commun.* **2017**, *80*, 20–23. [CrossRef]
7. Hakim, M.; Yoo, C.-Y.; Joo, J.H.; Yu, J.H. Enhanced durability of a proton conducting oxide fuel cell with a purified yttrium-doped barium zirconate-cerate electrolyte. *J. Power Sources* **2015**, *278*, 320–324. [CrossRef]
8. Muccillo, R.; Muccillo, E.N. Synthesis and Properties of $BaZr_{0.1}Ce_{0.7}Y_{02-x}M_xO_{3-\delta}$ (x = 0, 0.1; M = Dy, Yb) Compounds. *ECS Trans.* **2011**, *35*, 1251. [CrossRef]
9. Liu, Z.; Zhou, M.; Chen, M.; Cao, D.; Shao, J.; Liu, M.; Liu, J. A high-performance intermediate-to-low temperature protonic ceramic fuel cell with in-situ exsolved nickel nanoparticles in the anode. *Ceram. Int.* **2020**, *46*, 19952–19959. [CrossRef]
10. Shah, M.Y.; Mushtaq, N.; Rauf, S.; Akbar, N.; Xing, Y.; Wu, Y.; Wang, B.; Zhu, B. Advanced fuel cell based on semiconductor perovskite La–BaZrYO3-δ as an electrolyte material operating at low temperature 550 °C. *Int. J. Hydrog. Energy* **2020**, *45*, 27501–27509. [CrossRef]
11. Shah, M.A.K.Y.; Rauf, S.; Mushtaq, N.; Zhu, B.; Tayyab, Z.; Yousaf, M.; Hanif, M.B.; Lund, P.D.; Lu, Y.; Asghar, M.I. Novel Perovskite Semiconductor Based on Co/Fe-Codoped LBZY ($La_{0.5}Ba_{0.5}Co_{0.2}Fe_{0.2}Zr_{0.3}Y_{0.3}O_{3-\delta}$) as an Electrolyte in Ceramic Fuel Cells. *ACS Appl. Energy Mater.* **2021**, *4*, 5798–5808. [CrossRef]
12. Lu, Y.; Mi, Y.; Li, J.; Qi, F.; Yan, S.; Dong, W. Recent Progress in Semiconductor-Ionic Conductor Nanomaterial as a Membrane for Low-Temperature Solid Oxide Fuel Cells. *Nanomaterials* **2021**, *11*, 2290. [CrossRef]
13. Liu, Y.; Xia, C.; Wang, B.; Tang, Y. Layered $LiCoO_2$–$LiFeO_2$ Heterostructure Composite for Semiconductor-Based Fuel Cells. *Nanomaterials* **2021**, *11*, 1224. [CrossRef]
14. Xu, D.; Yan, A.; Xu, S.; Zhou, Y.; Yang, S.; Zhang, R.; Yang, X.; Lu, Y. Self-Assembled Triple ($H^+/O_2^-/e^-$) Conducting Nanocomposite of Ba-Co-Ce-YO into an Electrolyte for Semiconductor Ionic Fuel Cells. *Nanomaterials.* **2021**, *11*, 2365. [CrossRef] [PubMed]
15. Sailaja, J.M.; Murali, N.; Margarette, S.; Jyothi, N.K.; Rajkumar, K.; Veeraiah, V. Chemically stable proton conducting doped $BaCeO_3$ by citrate-EDTA complexing sol-gel process for solid oxide fuel cell. *S. Afr. J. Chem. Eng.* **2018**, *26*, 61–69.
16. Fabbri, E.; Bi, L.; Pergolesi, D.; Traversa, E. Towards the next generation of solid oxide fuel cells operating below 600 °C with chemically stable proton-conducting electrolytes. *Adv. Mater.* **2012**, *24*, 195–208. [CrossRef] [PubMed]
17. Stevens, J.; Wieczorek, W.; Raducha, D.; Jeffrey, K. Proton conducting gel/H_3PO_4 electrolytes. *Solid State Ion.* **1997**, *97*, 347–358. [CrossRef]
18. Yashima, M.; Tsujiguchi, T.; Sakuda, Y.; Yasui, Y.; Zhou, Y.; Fujii, K.; Torii, S.; Kamiyama, T.; Skinner, S.J. High Oxide-Ion Conductivity through the Interstitial Oxygen Site in $Ba_7Nb_4MoO_{20}$-Based Hexagonal Perovskite Related Oxides. *Nat. Commun.* **2021**, *12*, 556. [CrossRef] [PubMed]
19. Wang, B.B.; Zhong, X.X.; He, C.L.; Zhang, B.; Cvelbar, U.; Ostrikov, K. Solvent-dependent structures and photoluminescence of WO_{3-x} nanomaterials grown in nonaqueous solutions. *J. Alloy. Compd.* **2021**, *854*, 157249. [CrossRef]
20. Wang, Z.; Fan, X.; Li, C.; Men, G.; Han, D.; Gu, F. Humidity-sensing performance of 3DOM WO_3 with controllable structural modification. *ACS Appl. Mater. Interfaces* **2018**, *10*, 3776–3783. [CrossRef]
21. Shah, M.Y.; Rauf, S.; Zhu, B.; Mushtaq, N.; Yousaf, M.; Lund, P.D.; Xia, C.; Asghar, M.I. Semiconductor Nb-Doped SrTiO3 − δ Perovskite Electrolyte for a Ceramic Fuel Cell. *ACS Appl. Energy Mater.* **2021**, *4*, 365–375. [CrossRef]
22. Mushtaq, N.; Xia, C.; Dong, W.; Wang, B.; Raza, R.; Ali, A.; Afzal, M.; Zhu, B. Tuning the energy band structure at interfaces of the $SrFe_{0.75}Ti_{0.25}O_{3-\delta}$–$Sm_{0.25}Ce_{0.75}O_{2-\delta}$ heterostructure for fast ionic transport. *ACS Appl. Mater. Interfaces* **2019**, *11*, 38737–38745. [CrossRef] [PubMed]
23. Wang, B.; Cai, Y.; Xia, C.; Kim, J.S.; Liu, Y.; Dong, W.; Wang, H.; Afzal, M.; Li, J.; Raza, R.; et al. Semiconductor-ionic membrane of LaSrCoFe-oxide-doped ceria solid oxide fuel cells. *Electrochim. Acta* **2017**, *248*, 496–504. [CrossRef]
24. Shah, M.A.K.Y.; Zhu, B.; Rauf, S.; Mushtaq, N.; Yousaf, M.; Ali, N.; Tayyab, Z.; Akbar, N.; Yang, C.P.; Wang, B. Electrochemical properties of a co-doped $SrSnO_{3-\delta}$-based semiconductor as an electrolyte for solid oxide fuel cells. *ACS Appl. Energy Mater.* **2020**, *3*, 6323–6333. [CrossRef]
25. Mushtaq, N.; Lu, Y.; Xia, C.; Dong, W.; Wang, B.; Shah, M.Y.; Rauf, S.; Akbar, M.; Hu, E.; Raza, R.; et al. Promoted electrocatalytic activity and ionic transport simultaneously in dual functional $Ba_{0.5}Sr_{0.5}Fe_{0.8}Sb_{0.2}O_{3-\delta}$-$Sm_{0.2}Ce_{0.8}O_{2-\delta}$ heterostructure. *Appl. Catal. B: Environ.* **2021**, *298*, 120503. [CrossRef]
26. Shah, M.A.K.Y.; Mushtaq, N.; Rauf, S.; Xia, C.; Zhu, B. The semiconductor $SrFe_{0.2}Ti_{0.8}O_{3-\delta}$-ZnO heterostructure electrolyte fuel cells. *Int. J. Hydrog. Energy* **2019**, *44*, 30319–30327. [CrossRef]

27. Shah, M.Y.; Tayyab, Z.; Rauf, S.; Yousaf, M.; Mushtaq, N.; Imran, M.A.; Lund, P.D.; Asghar, M.I.; Zhu, B. Interface engineering of bi-layer semiconductor $SrCoSnO_{3-\delta}$-$CeO_{2-\delta}$ heterojunction electrolyte for boosting the electrochemical performance of low-temperature ceramic fuel cell. *Int. J. Hydrog. Energy* **2021**, *46*, 33969–33977. [CrossRef]
28. Chen, G.; Liu, H.; He, Y.; Zhang, L.; Asghar, M.I.; Geng, S.; Lund, P.D. Electrochemical mechanisms of an advanced low-temperature fuel cell with a $SrTiO_3$ electrolyte. *J. Mater. Chem. A* **2019**, *7*, 9638–9645. [CrossRef]
29. Katrib, A.; Hemming, F.; Wehrer, P.; Hilaire, L.; Maire, G. The multi-surface structure and catalytic properties of partially reduced WO_3, WO_2 and WC + O_2 or W + O_2 as characterized by XPS. *J. Electron Spectrosc. Relat. Phenom.* **1995**, *76*, 195–200. [CrossRef]
30. Efkere, H.I.; Gümrükçü, A.E.; Özen, Y.; Kınacı, B.; Aydın, S. Şebnem; Ates, H.; Özçelik, S. Investigation of the effect of annealing on the structural, morphological and optical properties of RF sputtered WO_3 nanostructure. *Phys. B Condens. Matter.* **2021**, *622*, 413350. [CrossRef]
31. Wang, B.; Zhu, B.; Yun, S.; Zhang, W.; Xia, C.; Afzal, M.; Cai, Y.; Liu, Y.; Wang, Y.; Wang, H. Fast ionic conduction in semiconductor $CeO_{2-\delta}$ electrolyte fuel cells. *NPG Asia Mater.* **2019**, *11*, 1–12. [CrossRef]